Understanding Orographic Effects on Surface Observations at Macquarie Island

ZHAN WANG

School of Earth, Atmosphere and Environment, Monash University, Monash, Victoria, Australia

DANIJEL BELUSIC*

Centre for Ecology and Hydrology, Wallingford, United Kingdom

YI HUANG AND STEVEN T. SIEMS

School of Earth, Atmosphere and Environment, Monash University, Monash, and Australian Research Council Centre of Excellence for Climate System Science, Melbourne, Victoria, Australia

MICHAEL J. MANTON

School of Earth, Atmosphere and Environment, Monash University, Monash, Victoria, Australia

(Manuscript received 20 October 2015, in final form 24 July 2016)

ABSTRACT

The meteorological observations on Macquarie Island have become of increasing value for efforts to understand the unique nature of atmospheric processes over the Southern Ocean. While the island is of modest elevation (peak altitude of 410 m), the orographic effects on observations on this island are still not clear. High-resolution numerical simulations [Weather Research and Forecasting (WRF) Model] with and without terrain have been used to identify orographic effects for four cases representing common synoptic patterns at Macquarie Island: a cold front, a warm front, postfrontal drizzle, and a midlatitude cyclone. Although the simulations cannot capture every possible feature of the precipitation, preliminary results show that clouds and precipitation can readily be perturbed by the island with the main enhancement of precipitation normally in the lee in accordance with the nondimensional mountain height being much less than 1. The weather station is located at the far north end of the island and is only in the lee to southerly and southwesterly winds, which are normally associated with drizzle. The station is on the upwind side for strong northwesterly winds, which are most common and can bring heavier frontal precipitation. Overall the orographic effect on the precipitation record is not found to be significant, except for the enhancement of drizzle found in southwesterly winds. Given the strong winds over the Southern Ocean and the shallow height of the island, the 3D nondimensional mountain height is smaller than 1 in 93.5% of the soundings. As a result, boundary layer flow commonly passes over the island, with the greatest impact in the lee.

1. Introduction

The Southern Ocean stretches from the edge of Antarctica to ~50°S and is covered by a highly pristine (Bates et al. 1998a; Gras 1995) and unique atmosphere. The region known as the ''furious fifties'' has the strongest annually averaged mean surface wind speed (Vinoth and Young 2011) and greatest fractional cloud cover (Mace et al. 2007) on Earth, as well as the most frequent precipitation over the global oceans (Ellis et al. 2009). Large biases in Earth's energy and water budget in global reanalysis and climate models have also been found over the Southern Ocean (Trenberth and Fasullo 2010); they are largely caused by an underestimation of low and midlevel clouds (Bodas-Salcedo et al. 2012) and a poor representation of precipitation processes (Li et al. 2013). In the past few years, this problem has become a frontline

* Current affiliation: Swedish Meteorological and Hydrological Institute, Norrköping, Sweden.

Corresponding author address: Steven T. Siems, School of Earth, Atmosphere and Environment, Monash University, Wellington Rd. and Blackburn Rd., Clayton, VIC 3800, Australia.
E-mail: steven.siems@monash.edu

DOI: 10.1175/JAMC-D-15-0305.1

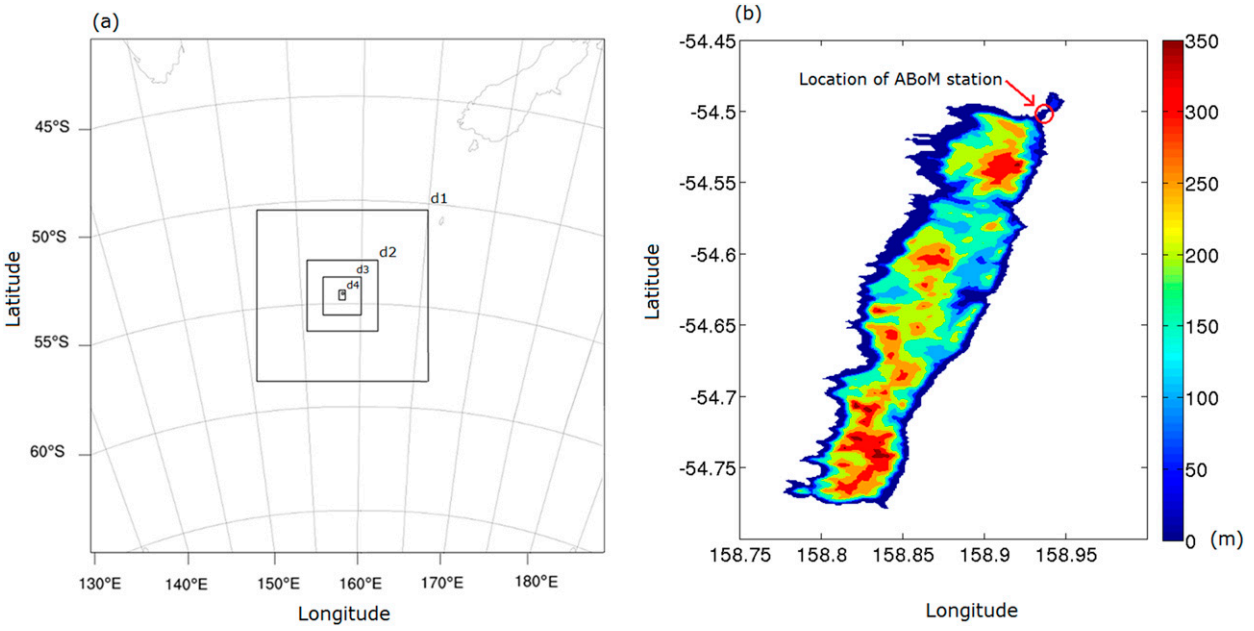

FIG. 1. (a) WRF domains used in this study, and (b) the topography of Macquarie Island from SRTM. The red circle shows the location of the ABoM station.

concern of the climate community to the point that the geosciences advisory panel to the U.S. National Science Foundation (Hornberger et al. 2014) specifically identified the atmospheric processes over the Southern Ocean under one of their four research frontiers.

In situ observations of the atmosphere over the Southern Ocean are relatively rare because of its remote location and harsh environment. They have generally been limited to infrequent, isolated field campaigns such as the first Aerosol Characterization Experiment (ACE-1; Bates et al. 1998b) and the Southern Ocean Cloud Experiments (SOCEX I and II; Boers et al. 1998; Boers and Krummel 1998), and other opportunities on board local ships (e.g., Kanitz et al. 2011) and aircraft with limited instrumentation (e.g., Huang et al. 2015; Chubb et al. 2013, 2016).

Macquarie Island (54.50°S, 158.94°E) is a small, remote island in the midst of the Southern Ocean (Fig. 1a) with a high-quality record of both surface and upper-air observations that have been maintained by the Australian Bureau of Meteorology (ABoM) and date back to 1948. These observations at Macquarie Island station (MAC) have become of great value in identifying climate trends over the Southern Ocean. Based on these records, Adams (2009) found a 35% increase in annual precipitation from 1970 to 2007, and Hande et al. (2012a) found the surface wind speed increased 4.26 cm s^{-1} yr^{-1} from 1973 to 2011.

These observations have also become of value in understanding the unique nature of the atmospheric processes over the Southern Ocean. For example, Hande et al. (2012b, 2015) found a decoupling structure near 800 m from the upper-air soundings at MAC. Huang et al. (2012) employed the MAC soundings to infer the common presence of boundary layer clouds. Recently Wang et al. (2015) compared the precipitation records from MAC with those from the reanalysis product [ERA-Interim (ERA-I); Dee et al. 2011], and found that ERA-I underestimates the average annual precipitation by approximately 6.8% from 1979 to 2011. These in situ observations will be of increasing value for many future field activities over the Southern Ocean, such as the proposed Southern Ocean Cloud Radiation and Aerosol Transport Experimental Studies (SOCRATES) campaign, where additional surface observations at Macquarie Island, including microwave radiometers and surface broadband radiometers, ground-based lidar, and boundary layer observations from unmanned aerial systems have been proposed (http://www.atmos.washington.edu/socrates/SOCRATES_white_paper_Final_Sep29_2014.pdf).

Given the importance of the surface and upper-air observations over Macquarie Island, it remains an open question as to what extent these local observations represent the meteorological conditions over the surrounding Southern Ocean. It is well appreciated that orography can readily perturb winds, cloud cover, and precipitation. In the Southern Ocean boundary layer, with the strong winds and high relative humidity, even modest orography has the potential to create such local perturbations. For example, the airborne observation in the Deep Propagating Gravity Wave Experiment (DEEPWAVE; Fritts et al. 2015) found strong high-altitude gravity waves

over the Southern Ocean that could be generated from even weak orographic forcing.

Commonly, the effect of orography on meteorological conditions has been expressed through the nondimensional mountain height ($H_m = Nh/U_c$), where U_c ($m\,s^{-1}$) is the cross-mountain wind speed, N (s^{-1}) is the Brunt–Väisälä frequency, and h (m) is the mountain height (Schär and Durran 1997; Baines 1998). For idealized two-dimensional flows, when the nondimensional mountain height is much less than 1, the current is forced over the mountain, leading to gravity waves and lee waves. When the nondimensional mountain height is much larger than 1, blocking is prevalent and the flow is disturbed horizontally rather than vertically. For isolated three-dimensional mountains, the nondimensional mountain height has been used as a key parameter to determine whether airflow passes over or around the mountain (e.g., Smolarkiewicz and Rotunno 1989).

The influence of orography on the distribution and intensity of precipitation, in particular, has long been recognized. For example, Browning et al. (1974) studied orographic effects on precipitation during the passage of cold fronts over west Britain. Smith (1979) showed that the orographic effect on precipitation over small hills is different from that over mountains, where the rainfall maximum is near the hilltop instead of the upslope region. Johansson and Chen (2003) analyzed 15 yr of precipitation records from 370 stations in Sweden and found that precipitation increased with wind speed on the upwind side and there was less variation in precipitation on the leeward side, where wind speed did not strongly affect the amount of precipitation. Houze (2012) detailed 12 different mechanisms that can influence orographic precipitation including upslope enhancement, blocking effects of the terrain, and the ''seeder–feeder'' mechanism.

Numerical simulations have been widely used to study the orographic effects on flow dynamics and precipitation. Idealized numerical studies (e.g., Miglietta and Buzzi 2001; Colle 2004) have shown that the flow field and the intensity and distribution of precipitation are sensitive to the nondimensional mountain height. Cannon et al. (2012) found from idealized numerical simulations that embedded convection over tall and wide mountains causes competing effects (enhanced condensation in updrafts and enhanced evaporation through turbulent mixing and compensating subsidence) and leads to little net change in precipitation, while, for short and narrow mountains, convective updrafts strongly enhance the precipitation efficiency. Watson and Lane (2012, 2014) undertook idealized, high-resolution simulations and found that a concave ridge generates substantially more precipitation than the straight and convex ridges. A number of real-world simulations have focused on the island of Hawaii (e.g., Rasmussen et al. 1989; Reisner and Smolarkiewicz 1994), where the 4-km mountain peak is found to create blocking with a large nondimensional mountain height. With ever increasing numerical capabilities, the resolutions of numerical simulations have become finer and finer. In many cases, high-resolution (~100 m) mesoscale simulations are necessary to capture the smaller-scale features that could influence the distribution of orographic precipitation (Nugent et al. 2014).

The aim of this study is to identify and appreciate biases that may exist in Macquarie Island records arising from orographic forcing. A series of high-resolution (100 m) numerical simulations have been undertaken to investigate orographic forcing across a range of common meteorological conditions (i.e., warm front, cold front, midlatitude cyclone, and nonfrontal transient drizzle). As the investigation is limited to these four cases, it is by no means comprehensive. Surface precipitation is the primary focus of these simulations, given its necessity in closing the energy and water budgets over the Southern Ocean, but the analysis is expanded to examine boundary layer winds, temperature, cloud cover, and the generation of gravity waves across the island.

2. The meteorological conditions of Macquarie Island

Macquarie Island is primarily a north–south-oriented narrow island, about 34 km long and 5 km wide (Jovanovic et al. 2012) (Fig. 1b). The peak elevation is 410 m and located on the southern portion of the island. The observation station is located near the northernmost part of the island on a narrow isthmus at an elevation of 6 m above sea level and is commonly exposed to the prevailing westerly winds (Hande et al. 2012b). Since the narrowest place of the island is the 150-m-wide isthmus in the north, we infer that a very high resolution (~100 m) is necessary for a numerical model to properly resolve terrain effects on the station observations (Nugent et al. 2014).

The climate of Macquarie Island is defined by the surrounding Southern Ocean, with a weak annual cycle of temperature (Streten 1988) and cloud cover (Huang et al. 2012). The temperature ranges from 5° to 13°C in January and from 1° to 9°C in July, and snow is common in winter (Streten 1988; Wang et al. 2015). There is no diurnal cycle or sea-breeze signature given the strong westerly winds. Most winds are from the west and northwest, and 88% of the 30-min mean surface wind speeds are higher than $5\,m\,s^{-1}$ from 2003 to 2011.

The meteorological conditions of Macquerie Island are dominated by the circumpolar storm track in the

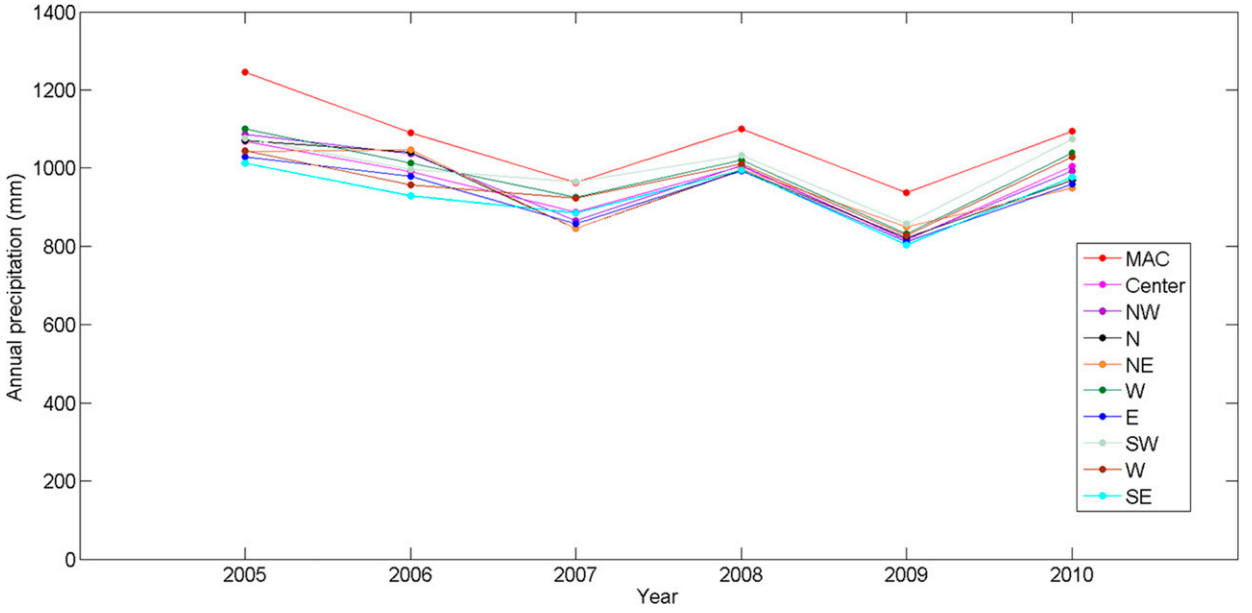

FIG. 2. Annual precipitation from MAC and nine ERA-I grids around Macquarie Island.

Southern Ocean (Simmonds and Keay 2000; Hoskins and Hodges 2005). Midlatitude cyclones or fronts pass across this island approximately every five or six days through the year; more frequently in the winter and less frequently in the summer (Streten 1988). According to Wang et al. (2015), cold fronts are found to contribute more than 40% of the precipitation above $1\,\mathrm{mm\,h^{-1}}$, and warm fronts contribute about 20%. Most precipitation arrives from the west, southwest, and northwest, but precipitation from the southwest is commonly drizzle. The frequency of the precipitation is 36.4% at the 3-h time scale from the station observations (the detection threshold is $0.067\,\mathrm{mm\,h^{-1}}$), while light precipitation ($P < 0.5\,\mathrm{mm\,h^{-1}}$) is encountered 29.7% of the time. These frequencies were greater than those found in both the ERA-I and *CloudSat*-based products, but ERA-I produces a considerable amount of drizzle (43.9%), which is weaker than the detectable threshold of MAC ($0.067\,\mathrm{mm\,h^{-1}}$). Heavy precipitation ($P > 1.5\,\mathrm{mm\,h^{-1}}$) is encountered 1.1% of the time. Wang et al. (2015) detailed that from 1979 to 2011 the average annual MAC precipitation (1023 mm) was 6.8% greater than that from ERA-I (953 mm). This underestimate is consistently found in the eight surrounding ERA-I grids (0.75° × 0.75°) for 2005–10 (Fig. 2).

3. Methodology

The Weather Research and Forecasting (WRF) Model (version 3.5) is a sophisticated numerical model that solves the nonhydrostatic Euler equations in a terrain-following coordinate system (Skamarock and Klemp 2008). In this study, five domains centered on Macquarie Island with one-way nesting are configured with 70 vertical levels extending from the surface to 5000 Pa over the ocean. The first five levels from the surface are set at 10, 41, 91, 152, and 214 m, and the vertical spacing continues to increase with the height to the top. The nested horizontal grid spacings of 9000, 3000, 1000, 333.33, and 111.11 m are set for domains of 100 × 100, 100 × 100, 199 × 199, 150 × 100, and 100 × 100 grid points, respectively. The Year of Tropical Convection (Moncrieff et al. 2012) data (1.25° × 1.25° grid, 91 pressure levels, and 6-hourly updates) are used for initialization and boundary conditions. Simulations were configured with the Rapid Radiative Transfer Model for GCMs (RRTMG) shortwave and longwave radiation scheme (Mlawer et al. 1997; Iacono et al. 2008), the Noah land surface model (Chen and Dudhia 2001), the Yonsei University (YSU; Hong and Lim 2006) planetary boundary layer scheme, the Thompson (Thompson et al. 2008) microphysical scheme, and the Kain–Fritsch cumulus scheme (Ma and Tan 2009). Note that the cumulus scheme is used only on the coarsest domain. This setup has been chosen based on the previous WRF simulations over Tasmania and the Southern Ocean in Huang et al. (2014). Terrain information is from the Shuttle Radar Topography Mission (SRTM; Farr et al. 2007), which includes digital topographic data for 80% of Earth's land surface between 60°N and

TABLE 1. A summary of the case-study simulations. Parameters are from models in their highest resolutions.

Case	Model start date	Time of simulation (h)	Wind direction at 500 m MSL	Highest resolution (m)	Mean wind speed 50–250 m MSL ($m\,s^{-1}$)	Mean N (s^{-1})	H_m
Cold front	9 Oct 2008	24	NW	100	18.3	0.0171	0.19
Warm front	14 Mar 2010	36	W	100	7.06	0.0154	0.54
Drizzle	30 May 2009	36	SW	100	14.8	0.0128	0.21
Cyclone	6 May 2009	24		1000	6.8	0.0154	0.42

56°S. For Macquarie Island, the horizontal resolution is 90 m.

Neither the Reynolds-averaged Navier–Stokes equation (RANS) models nor the large-eddy simulation models are fully appropriate for high-resolution simulations with the grid spacing of several hundred meters, as the size of energy-containing eddies are close to the model filter scale (Wyngaard 2004). Nevertheless, here we use the YSU scheme as a RANS-type turbulence closure for the innermost domain. In the YSU scheme, the turbulent fluxes in each model grid are estimated from the mean atmospheric variables and their gradients using the eddy diffusion equations. Nonlocal fluxes are also introduced in a parameterized nonlocal term (Hong and Lim 2006). Since the nesting is one way, the spatial structures are always compared with lower-resolution domains for consistency. The innermost domain is used only for exploration of the close surroundings of the weather station in two contrasting simulations: with and without terrain.

Four case studies (Table 1)—namely, a cold front, a warm front, drizzle, and a midlatitude cyclone—have been chosen to represent the common synoptic meteorology/precipitation types (Wang et al. 2015). Because of limited space, only the cold- and warm-frontal cases are presented in detail, as they are often associated with strong precipitation (Catto et al. 2012). The "cyclone" category differs from the frontal categories in terms of the significant wind pattern changes over the station associated with the passage of the low center. The four cases were simulated both with and without the Macquarie Island terrain in all domains such that any orographic effects on the airflow field and distribution and intensity of precipitation can be isolated. Presented results are from 12 h after the initialization of the model unless stated otherwise. A 20-min time interval is chosen for the accumulation of precipitation. Both surface observations (Table 2) and upper-air soundings (twice a day at 0000 and 1200 UTC) are employed to evaluate the simulations.

The mean N and mean wind speed U_m from 50 to 250 m over the MAC site location in no-terrain simulations were used to calculate the nondimensional mountain height. Theoretically, the nondimensional mountain height is calculated in a 2D framework using the cross-mountain wind speed, which is in our case the wind component perpendicular to the island range ($U_c = U_m \sin\beta$, where β is the angle between the wind vector and the main line of the island range with a heading of 279°). While such a perspective may be appropriate for the orographic forcing about the island as a whole, it is of limited meaning for a station located on the far northern tip of the island. In our case studies, the 2D nondimensional mountain height is used to study the terrain effects of the whole island. The 3D nondimensional mountain height is calculated using mean wind speeds instead of the cross-mountain wind speeds to estimate the terrain effects of the 250-m ridge immediately to the southwest of the station and the hill to the north. The mountain height h used in the calculation is 250 m.

The moist N was calculated using the expression in Kirshbaum and Durran (2004):

$$N_m^2 = \frac{g}{T}\left(\frac{dT}{dz} + \Gamma_m\right)\left(1 + \frac{Lq_s}{RT}\right) - \frac{g}{1+q_w}\frac{dq_w}{dz},$$

where T is the temperature, R is the ideal gas constant for dry air, L is the latent heat of condensation of water, q_s is the saturation mixing ratio, q_w is the total water mixing ratio, and Γ_m is the moist adiabatic lapse rate.

4. Results

In recent years, a number of studies have been undertaken using numerical simulations of clouds and

TABLE 2. Instruments of the MAC surface observations.

Parameters	Instruments
Surface air temperature	Dobbie dry-bulb mercury thermometer on 2 m AGL
Surface pressure	Vaisala PTB220B barometer
Wind directions	Synchrotac cups type 732 anemometer on 10 m AGL
Wind speeds	Synchrotac cups type 732 anemometer on 10 m AGL
Precipitation	Rimco tipping-bucket rain gauge
Snow	203-mm (8 in.) or 200-mm-capacity snow gauge

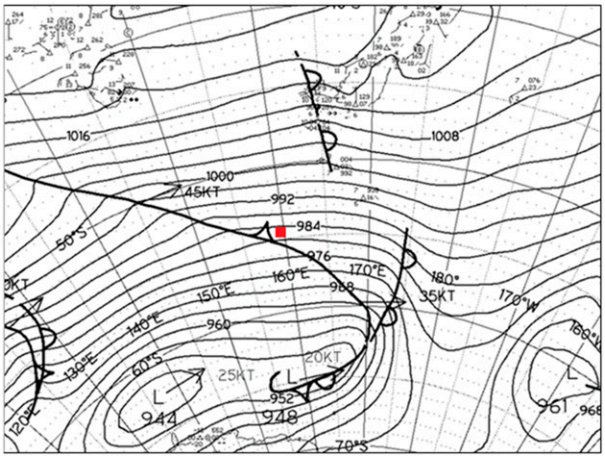

FIG. 3. The ABoM MSLP chart showing a cold front passing Macquarie Island (the red point) at 1200 UTC 9 Oct 2008.

precipitation over the Southern Ocean in the neighborhood of Tasmania (Morrison et al. 2010; Huang et al. 2014, 2015). These simulations have demonstrated limited skill in representing the boundary layer structure, including cloudiness, commonly citing a lack of skill in the reanalysis products employed for model initialization. Not surprisingly, the simulations presented herein also show limited skill in replicating some aspects of the surface observations, particularly precipitation. As our primary motivation is to study the orographic forcing, cases were selected to represent the common synoptic patterns that give rise to various types of precipitation. Errors in the timing and intensity of the precipitation are neither surprising nor of primary interest in this study.

a. Passage of a cold front

A cold front passed Macquarie Island from the west on 9 October 2008 (Fig. 3) sometime after 1200 UTC, according to the mean sea level pressure (MSLP). The surface observations of winds and pressure suggest that the major shift arrived at approximately 1600 UTC (Fig. 4) with a weaker, secondary shift arriving 4 h later at 2000 UTC. Ryan and Wilson (1985) reported similar multistage periods of convection during the passage of cold fronts over the Southern Ocean, consisting of prefrontal midlevel cloud bands and a postfrontal low-level cloud band. The core of the cyclone is far to the south of MAC near the Antarctic coast, and a high pressure system is located over the Tasman Sea far to the north of the island. Such an elongated cold front is relatively rare over the Southern Ocean, as it is most common for the cyclonic core to be embedded in the storm track. This case study does, however, offer an ideal, isolated frontal passage for study.

The Moderate Resolution Imaging Spectroradiometer (MODIS; Platnick et al. 2003) image of cloud-top temperature at 2345 UTC reveals thick, cold (<228 K) cloud across the Tasman Sea (Fig. 5a). Lower/warmer and more

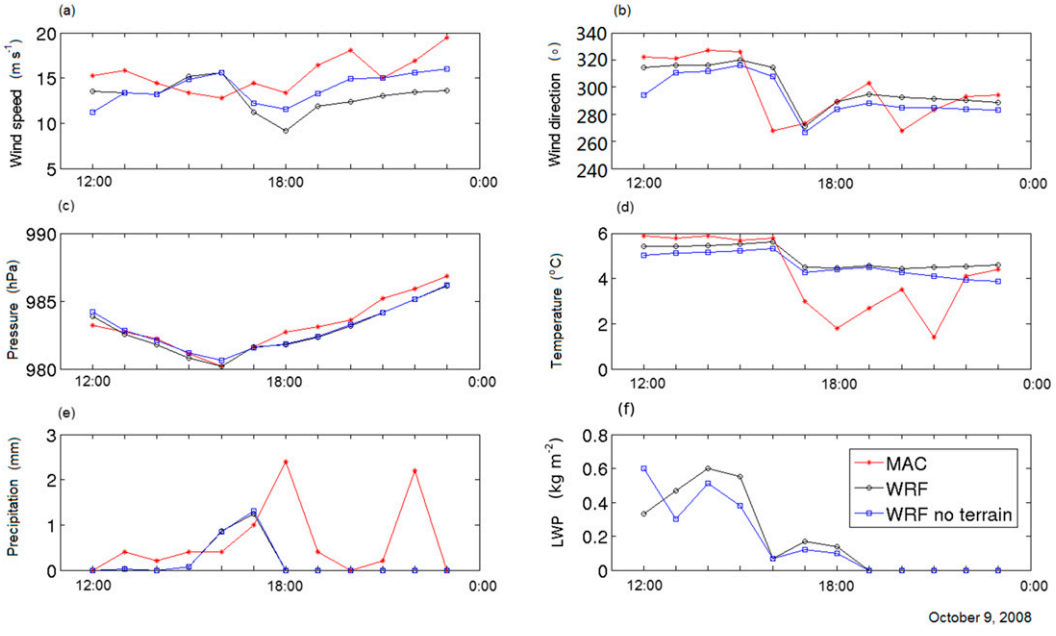

FIG. 4. (a) The 10-m wind speed (m s^{-1}), (b) wind direction (°), (c) surface pressure (hPa), (d) 2-m temperature (°C), (e) surface precipitation (mm), and (f) liquid water path (kg m^{-2}) from surface weather records (MAC) and 100-m-resolution WRF simulations with and without terrain for the cold-frontal case on 9 Oct 2008.

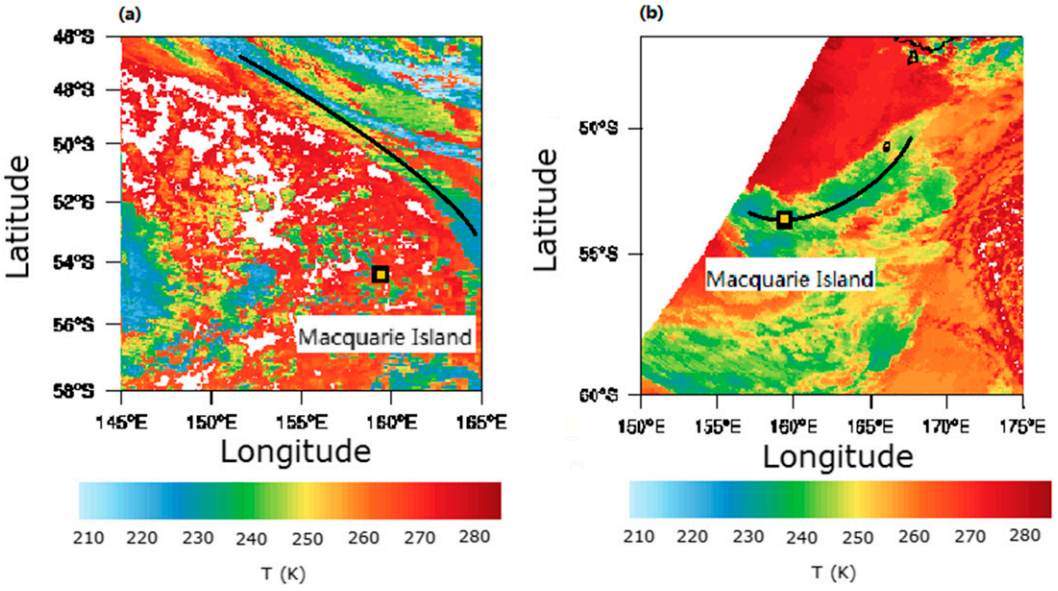

FIG. 5. Cloud-top temperature (K) from MODIS for (a) the cold-frontal case at 2345 UTC 9 Oct 2008 and (b) the warm-frontal case at 2200 UTC 14 Mar 2010. Black lines show the location of fronts.

broken cloud fields lie behind the main frontal clouds, which had passed Macquarie Island at the time of the image. The MAC sounding (Fig. 6a) is taken through a heavy prefrontal cloud band at 1200 UTC 9 Oct 2008, which is roughly 4 h before the front arrives. Saturation is observed through the boundary layer up to a weak inversion, located near 850 hPa, with a moist free troposphere extending to over 600 hPa. Strong [~60 kt (1 kt = 0.51 m s^{-1})] westerly winds are recorded through the depth of the troposphere, as are common over the Southern Ocean (Hande et al. 2012a).

These limited MAC observations are now employed to evaluate WRF simulations (with terrain). Looking first at the prefrontal (1200 UTC) sounding (Fig. 7a), we see that the simulation similarly produces a saturated environment up to roughly 850 hPa, albeit a few degrees colder. The free troposphere air immediately above the inversion is drier than observed. The simulated winds are roughly consistent with those observed. The convective available potential energy (CAPE) from MAC (0 J kg^{-1}) is lower than that in the simulation (6.2 J kg^{-1}), which is also demonstrated by the equivalent potential temperature profiles below 1 km (Fig. 6b). It is possible that there are important physical processes that are not being represented in the simulations. For example, it is possible that ice falling from upper-level clouds could create a seeder–feeder effect to initiate/enhance precipitation, particularly in the neighborhood of the fronts embedded in the storm track. The limited in situ and remote observations available are not sufficient to either confirm or reject such a hypothesis.

In now looking at the simulated surface-meteorological conditions (Fig. 4), some discrepancies are immediately evident. The timing of the initial frontal passage at 1600 UTC is captured reasonably well, but the intensity of the simulated temperature drop and wind shift is somewhat weaker than observed. Also the peak precipitation rate is roughly half of that observed and is approximately an hour too early. However, the secondary shift in the winds and temperature is completely missed in the WRF simulation. No precipitation was simulated through this time, either, contrary to observations. This missing of the secondary precipitation and temperature shift (Ryan and Wilson 1985) may result from the limited representation of the postfrontal low-level cloud band. During the postfrontal period (not shown), neither simulation produces any cloud field or precipitation, yet for this case study, the MODIS imagery (Fig. 5a) clearly reveals warm, low-level clouds in the postfrontal environment. Huang et al. (2014) noted difficulty in WRF simulation of boundary layer clouds over the Southern Ocean in the neighborhood of Tasmania. They suggested that the model deficiency may be associated with the insufficient surface moisture flux.

As a general summary, the WRF simulation is able to capture the major meteorological aspects of this frontal passage, although the simulation underestimates the amount of surface precipitation and it completely fails to capture a second stage to the frontal passage.

Leaving the physical observations behind, the sensitivity of the WRF simulations to the terrain is now explored. First and foremost, no significant difference is

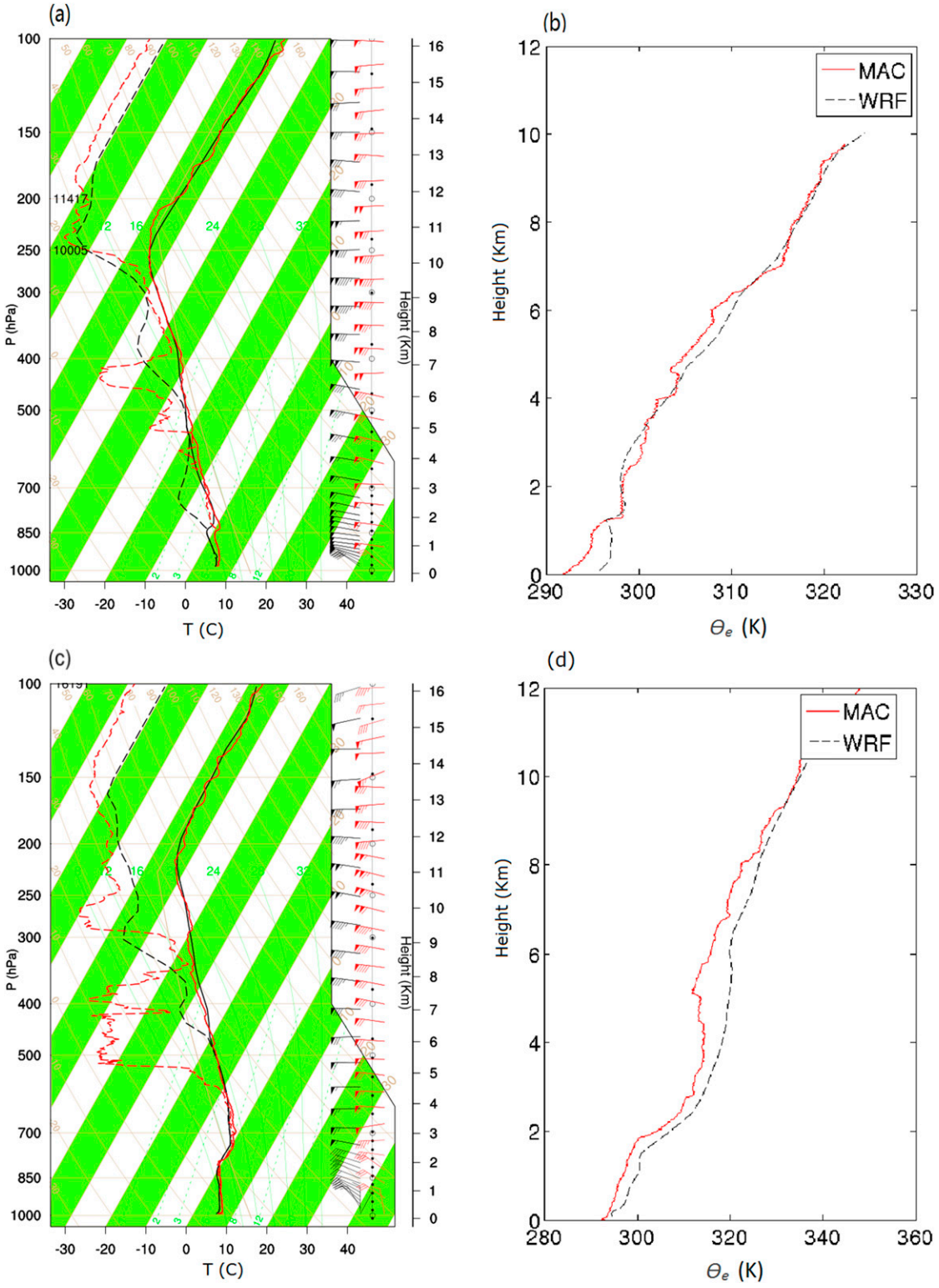

FIG. 6. (a) Skew *T* chart from the sounding (red) and 100-m-resolution WRF simulation with the terrain (black) for the cold-frontal case at 1200 UTC 9 Oct 2008, and (b profiles of equivalent potential temperature from MAC and the 100-m-resolution WRF simulation at the same time. (c),(d) As in (a) and (b), but for the warm-frontal case at 2300 UTC 14 Mar 2010.

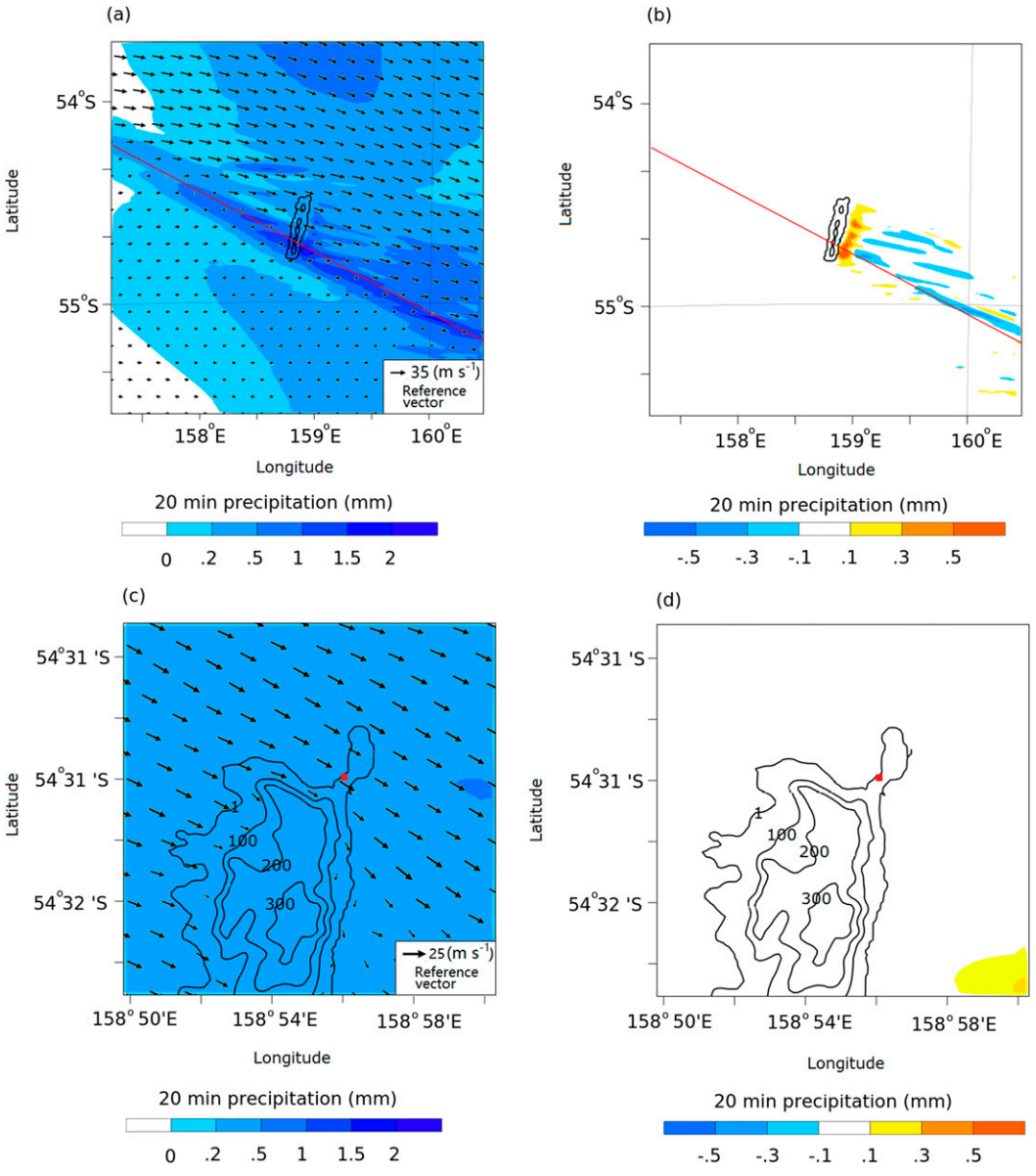

FIG. 7. Precipitation and wind fields from WRF simulations for the cold-frontal case at 1600 UTC 9 Oct 2008. (a) The 20-min surface accumulated precipitation and the wind field from the 1-km domain at 300 m above ground. (b) The differences of the precipitation between the simulations with and without terrain for the same domain (using precipitation in the no-terrain simulation subtracted from precipitation in the terrain simulation). Red lines denote the cross sections shown in Fig. 8 below. (c),(d) The corresponding precipitation and surface wind field from the 100-m domain at 50 m above ground. The red squares mark the location of the MAC station. The black contours are the topography (m).

observed in the surface precipitation through the duration of the simulations. Weak differences are apparent in the winds and temperature, with wind speeds arguably showing the greatest difference between the terrain and no-terrain simulations. In particular, the winds shift to a more westerly heading after the initial frontal passage at 1600 UTC. The simulated liquid water path above the station is also examined, although there are no physical observations available for evaluation purposes. It is interesting that in the simulated liquid water path is reduced after the frontal passage at 1600 UTC, as well as the discrepancies between the two simulations. These differences effectively cease with the frontal passage at 1600 UTC, with only weak differences thereafter. The simulations produce virtually no clouds after 1900 UTC, consistent with the absence of any surface precipitation.

The orographic effects on the precipitation distribution and the wind field are evident in the lee of the island at the time of frontal passage at 1600 UTC (Fig. 7). The accumulated precipitation over 20 min is presented to smooth over high-frequency oscillations yet still be short enough to reflect the connection to the dynamics. The simulated front arrives from the west with relatively intense precipitation, separating the wind field into two regions (Fig. 7a). Although there is no difference in simulated precipitation at the MAC station with or without terrain, the precipitation is enhanced immediately in the lee of the island and reduced further downwind (Fig. 7b) when the terrain is included. Figure 7c shows the wind field and precipitation (and Fig. 7d shows the precipitation difference) from the highest-resolution domain (100 m), noting no difference in the immediate neighborhood of the surface site.

To better understand the mechanism of the downwind orographic enhancement on the precipitation, two cross sections are drawn across the front (indicated in Fig. 7). A shallow convective system associated with warm rain below 1 km (Fig. 8a), the liquid water below 2 km (Fig. 8c), the ice between 4 and 6 km (Fig. 8e), and the upward vertical motion (Fig. 8g) is passing over the island from the west. We can see the leeside enhancement of the precipitation simulation with terrain (Fig. 8a). Differences in the leeward rain field are closely correlated to the differences in the warm cloud field (Figs. 8d,f). Looking at the vertical velocity (Fig. 8e), we see that the island sets off relatively weak gravity waves in the lee of the island. These gravity waves propagate roughly 60 km downwind from the island in the simulations (Fig. 8e) accounting for the differences in the cloud field and the precipitation. The enhancement of precipitation caused by leeside convergence is consistent with the enhanced clouds and ice over the top of island and transported by the strong wind. The 3D nondimensional mountain height in this case is 0.19, which is consistent with precipitation advection as well as the widespread gravity waves on the downwind side.

b. *Warm-frontal case study*

A warm front crossed Macquarie Island between 14 and 15 March 2010, arriving from the northwest at roughly 0000 UTC (Fig. 9a). (The ABoM MSLP chart for this case has been omitted, as no warm front was included given the remote location over the Southern Ocean.) At this time, the core of the cyclone is about 4° to the west of Macquarie Island (Fig. 9b). The MODIS image (2200 UTC 14 March 2010) reveals cloud-top temperatures below 252 K over Macquarie Island, presumably from the large-scale ascending motion (Fig. 5b).

From the 2300 UTC 14 March 2010 sounding (Fig. 6c), a temperature inversion is evident around 2 km (~800 hPa). Below this inversion, the air is saturated and stable. Above this inversion, the air remains saturated with the cloud field extending to heights of over 4 km. Accordingly, the CAPE and convective inhibition (CIN) are both $0\,J\,kg^{-1}$. The wind direction changes from northwest to west from the surface to 2-km height and then remains westerly through the rest of the free troposphere.

Focusing on the surface observations (Fig. 10), the precipitation begins at 1600 UTC and reaches the maxima ($2.7\,mm\,h^{-1}$) at 0000 UTC, then decreases dramatically. The surface winds are from the west before 1800 UTC and then briefly become weak westerly ($<5\,m\,s^{-1}$) and northerly in a transient wind field until 2200 UTC. After the warm front passes Macquarie Island at ~2300 UTC, the wind direction changes once more from the north back to the west, and the wind speed increases to above $10\,m\,s^{-1}$ (Fig. 10a). Later, at 0800 UTC, the surface winds peak at $\sim 20\,m\,s^{-1}$. As the warm front approaches the station from 2000 UTC 14 March to 0000 UTC 15 March, the surface temperature increases from 4° to 8°C. The pressure decreases throughout much of this 24-h period from 1005 to 985 hPa, reflecting the approaching cyclonic core.

Using these limited observations to evaluate the WRF simulation, we note the strong agreement in the sounding from the surface up to heights of 4 km (Fig. 6c). Above this height, the simulation is too moist, with clouds inferred up to the further height of 6 km. The deeper cloud in the WRF simulation did not, apparently, lead to more precipitation. The simulated precipitation is largely consistent with the observations, although the peak intensity is slightly underestimated ($2.0\,mm\,h^{-1}$) and arrives an hour earlier at 2300 UTC. The simulated pressure and temperature agree well with the observations. The profile of equivalent potential temperature is slightly overestimated by the simulation below 10 km (Fig. 6d).

The simulation shows some skills in reproducing the surface wind (Fig. 10a) except the wind direction shift occurred slightly earlier than observed (Fig. 10b), and the simulated wind direction shift with terrain is 1 h ahead of that without terrain. Looking at the difference between the simulations, the northerly wind is evidently blocked by the island from roughly 2100 to 2300 UTC, as seen from the lower wind speed with the terrain. Both the pressure and the temperature from the simulation and MAC match well (Figs. 10c,d). The two simulations show that the clouds above the station are enhanced by the terrain (Fig. 10f), especially when the winds are from the north, with liquid water path increased by $0.4\,kg\,m^{-2}$ at 0000 UTC.

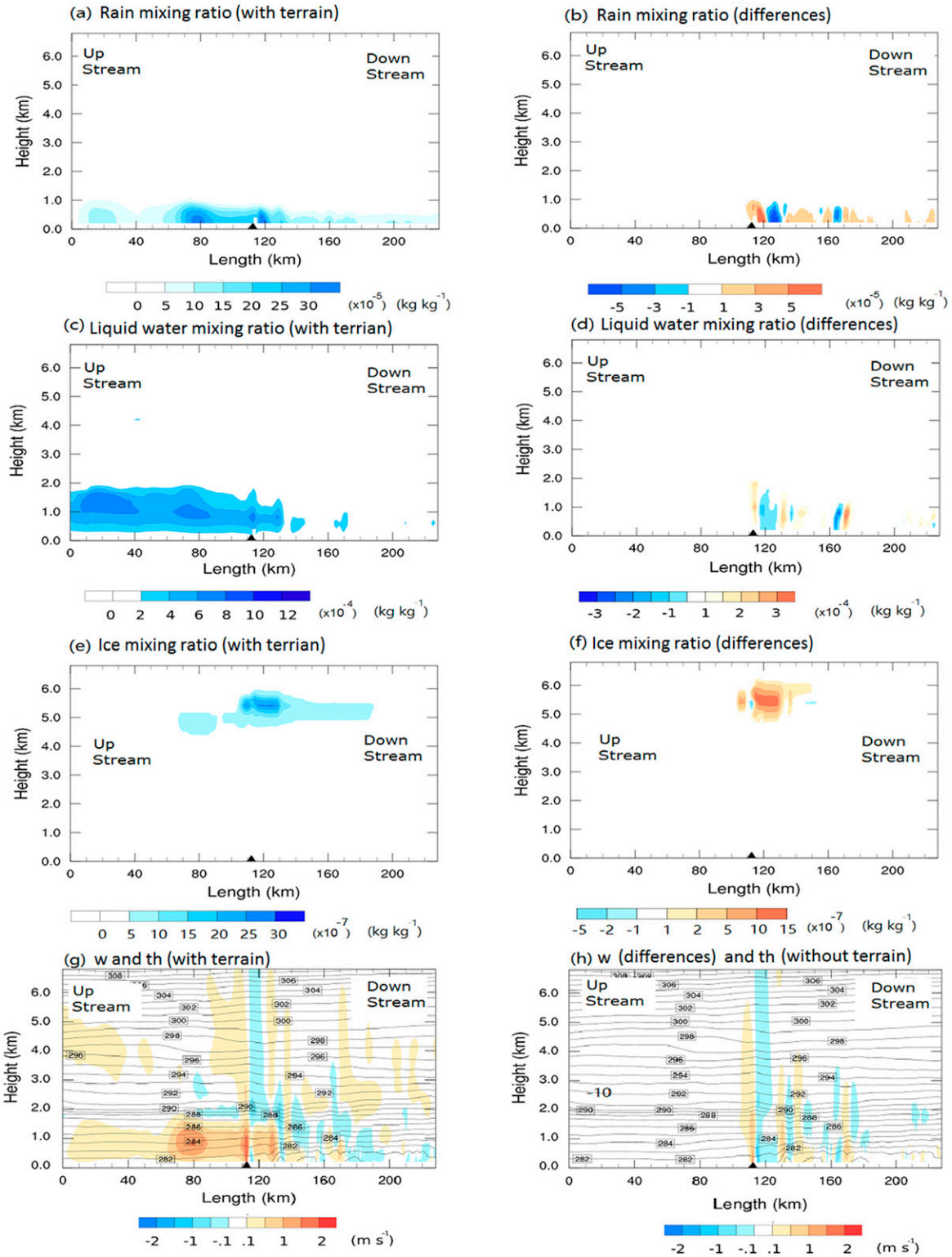

FIG. 8. The (a) rain, (c) liquid, and (e) ice mixing ratios and (g) the vertical wind speed (shading) and potential temperature (contours) cross sections from the 1-km-domain simulation with terrain in the cold-frontal case at 1600 UTC 9 Oct 2008. (b),(d),(f),(h) The corresponding differences between the simulations with and without terrain. The black triangle on the *x* axis indicates the location of Macquarie Island.

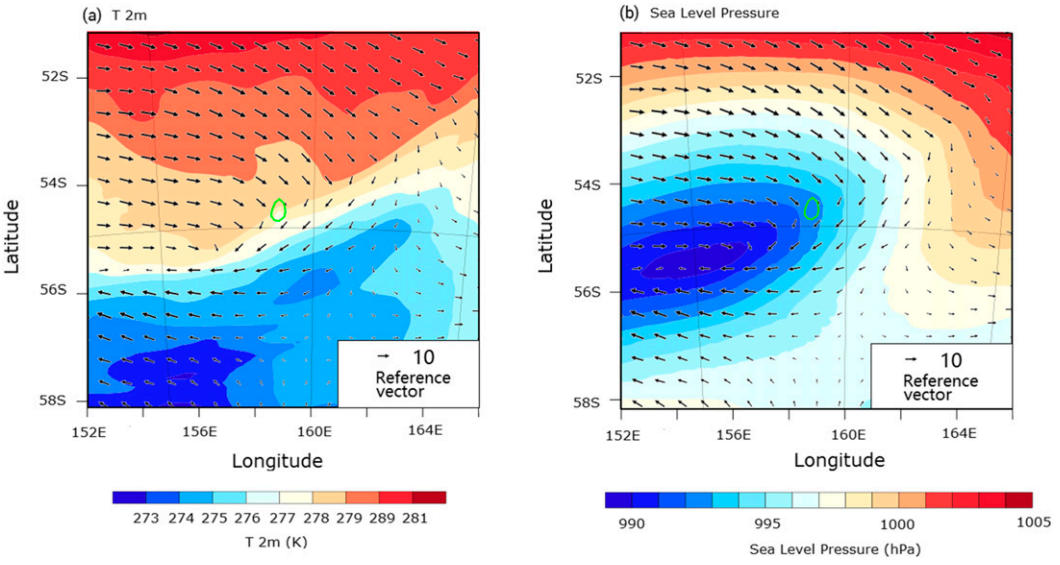

FIG. 9. (a) The 2-m temperature (K) and (b) MSLP (hPa) of the warm front passing Macquarie Island (the green oval) at 0000 UTC 15 Mar 2010.

As before, the orographic effect is isolated by running two sets of simulations: with and without terrain. Again, the terrain effects are negligible on the surface precipitation at the station except for a slight enhancement from 2200 to 0000 UTC (Fig. 10e) when the winds are from the north and northeast. Overall, the terrain effects in this case are stronger than in the first case, but the accumulated precipitation is only increased by approximately 5%, although the peak is increased by 12% in the 100-m simulations at 2200 UTC. In the 1000-m simulations (not shown), the accumulated precipitation is enhanced by 12% and the peak is enhanced by 16%.

An orographic effect is modeled on the surface precipitation immediately in the lee of the island, similar to the cold-frontal case (Fig. 11). At 2320 UTC, the warm front has just passed over the island and the wind has shifted back to the northwest and west. Precipitation is enhanced immediately downwind of the island. Consistent with the

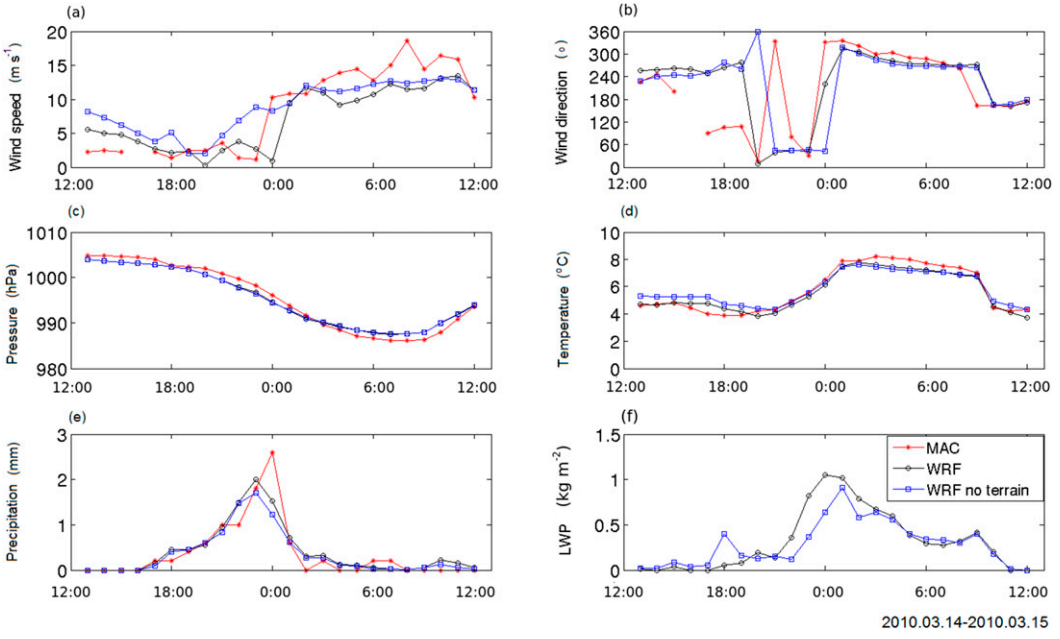

FIG. 10. As in Fig. 4, but for the warm-frontal case on 14 and 15 Mar 2010.

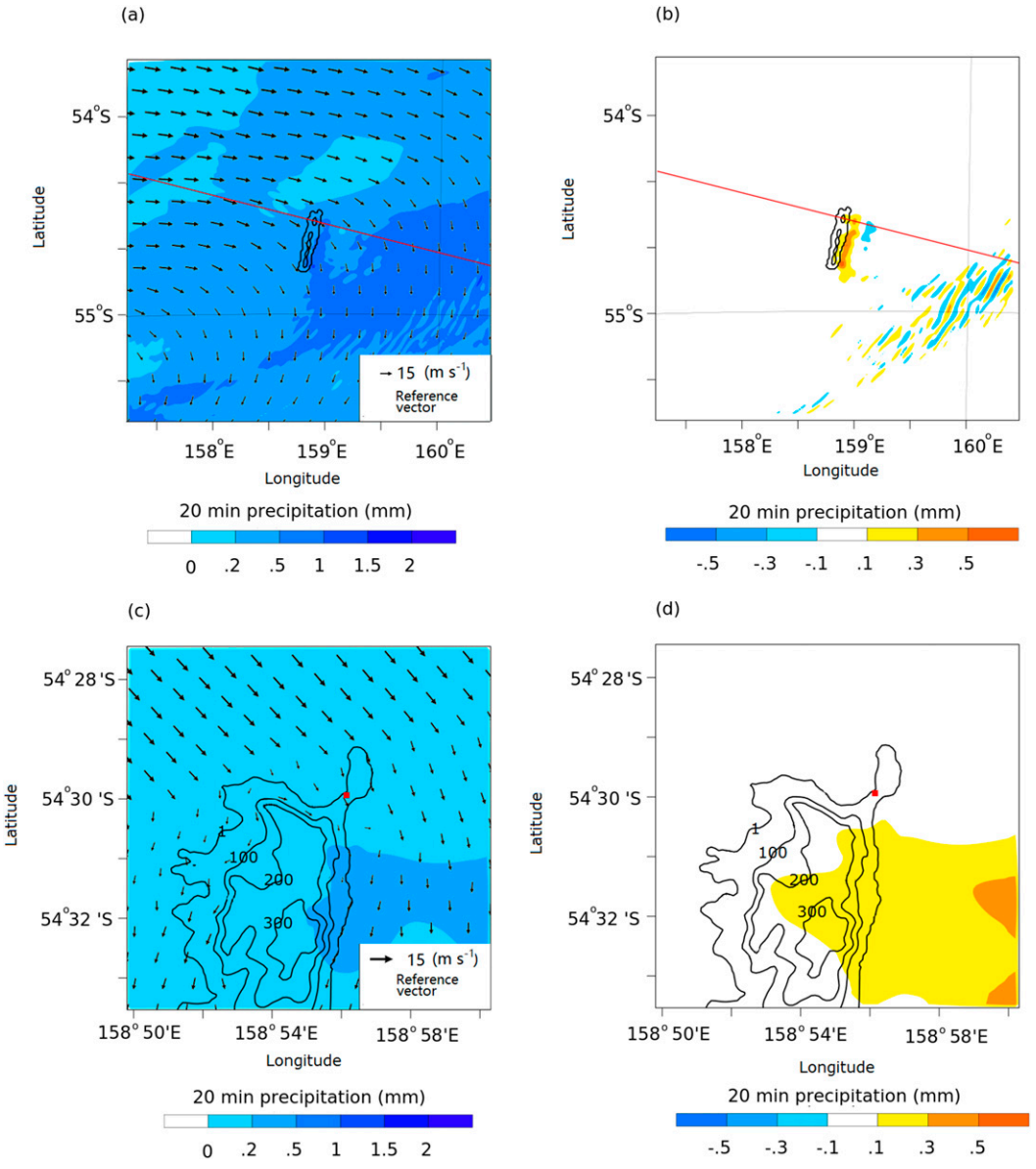

FIG. 11. As in Fig. 7, but for the cold-frontal case at 2320 UTC 14 Mar 2010. Red lines denote the cross sections shown in Fig. 12 below.

single point comparison (Fig. 10), the MAC station is near the region of precipitation enhancement but is largely unaffected (Fig. 11d). The wavelike pattern in the lower-right part of Fig. 11b is caused by the horizontal displacement of the main convection system between the two simulations.

As before, the structure of the frontal system at 2320 UTC is further explored through a cross section along the mean post frontal wind (Fig. 12). Downwind of the island, the simulations produce very shallow clouds and warm rain in the lowest kilometer and ice clouds between 3 and 7 km. Upwind of the island, the warm air is pushing up over the colder boundary layer air and clouds climb above 2 km in depth (Fig. 12c). The airflow upstream is weakly blocked by the island (Fig. 12h), which causes weak vertical motions that appear from approximately 10 km upwind from the island. Stronger vertical motions are triggered directly over the island, with clouds, ice, and precipitation advected to the lee. The gravity waves are weaker and have not propagated far downwind horizontally along this cross section. We note that, given the strong wind shifts occurring through this case study, the "downwind" section of the cross section does not capture the air mass that had passed over the island.

The 3D nondimensional mountain height is 0.54 for this warm-frontal case at 2300 UTC, which is considerably

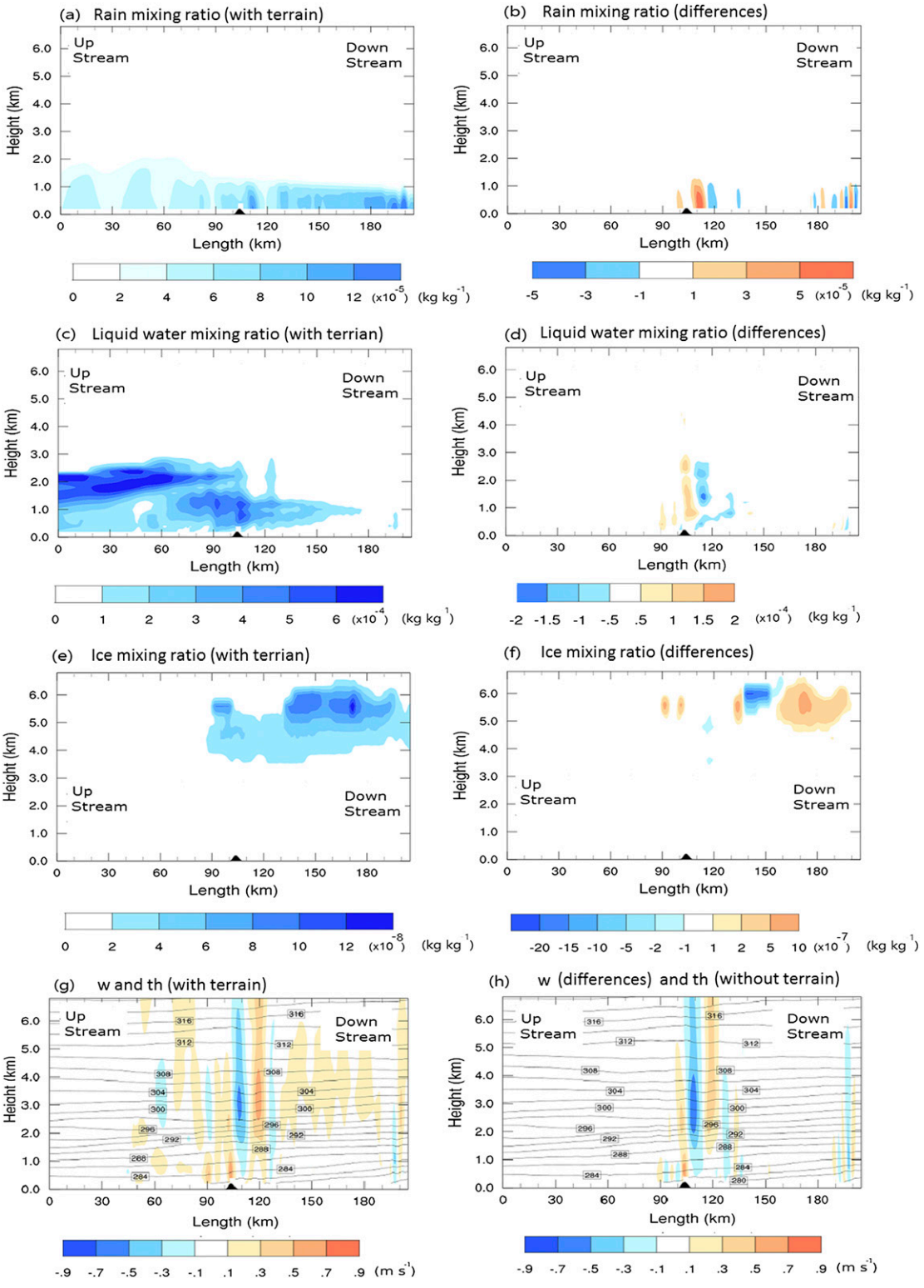

FIG. 12. As in Fig. 8, but for the warm-frontal case at 2320 UTC 14 Mar 2010.

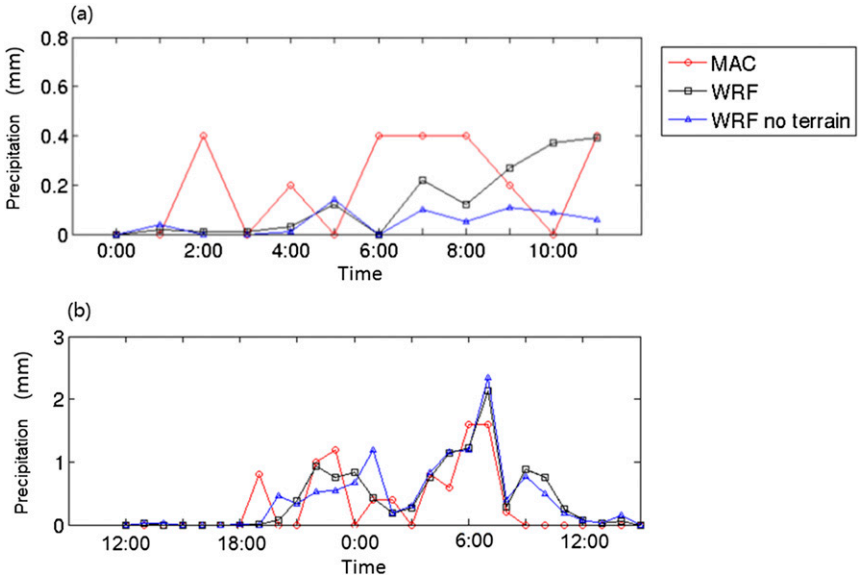

FIG. 13. Precipitation from the surface weather records (MAC) and WRF simulations with and without terrain in (a) the drizzle case from 0000 UTC 30 May 2009 and (b) the cyclone case from 1200 UTC 5 May 2009.

larger than for the first case study. Looking at a later time (0400 UTC, not shown), gravity waves are observed to have propagated approximately 60 km downwind.

c. *Drizzle and cyclonic-low case studies*

In the first two case studies, winds arrive from the open ocean to the west and northwest. The strong winds effectively reduce the nondimensional mountain height, and the dominant orographic features are, accordingly, located downwind of the station. No significant orographic effect is found on the surface precipitation at the station under these conditions in the WRF simulations. These cases also represent the two primary synoptic patterns that produce precipitation over Macquarie Island according to Wang et al. (2015). Further, "heavy" precipitation events ($P > 1\,\mathrm{mm\,h^{-1}}$ over a 3-h period) have been primarily observed to arrive from the west and north. Wang et al. (2015) noted that weaker precipitation (drizzle) is commonly observed with air arriving from the southwest. Also, a "cyclonic low" has been specifically identified when a low passes nearly overhead of Macquarie Island. These cases have been fully explored but are only summarized herein as they contribute less than 20% of the annual precipitation total at the station (Wang et al. 2015).

Drizzle cases commonly arise in the postfrontal period hours, probably because of shallow convection. On 30 May 2009, Macquarie Island was on the outskirts of a high pressure system located to the west of the island. The mean wind speed was about $15\,\mathrm{m\,s^{-1}}$ with the wind direction from southwest (240°), and the 3D nondimensional mountain height was as small as 0.21. Sporadic drizzle was recorded at the station often at the level of detection ($0.2\,\mathrm{mm\,h^{-1}}$). Very shallow roll clouds were observed in the MODIS imagery (not shown) most likely arising from the advection of cold southerly air over warmer sea surface temperatures (Kuettner 1971; Brown 1980). The high-resolution WRF simulations have some skill in capturing these dynamics. The simulated precipitation, however, is commonly weaker than that observed at the station (Fig. 13a) and much weaker than that of the earlier cold- (Fig. 4) and warm-frontal case studies (Fig. 10).

Focusing on the orographic effect on the simulated precipitation, a substantial enhancement is found over the last 6 h of the simulation (Fig. 13a). In this case, the main body of the island is upwind of the station, especially the ridge to the immediate south and west, with only weak blocking. The simulated winds cross over the island with precipitation enhanced along the eastern side (not shown).

Finally, the orographic forcing present when a cyclone passes over Macquarie Island is considered for the meteorological conditions of 5 and 6 May 2009. Normally cyclones arrive at Macquarie Island from the west and can be divided into two parts around the point of lowest pressure. First, the warm band, which is normally from the northwest, reaches the island. If the wind speed is high enough (e.g., $13\,\mathrm{m\,s^{-1}}$ for 6 May), the orography of the island will cause leeside convergence of the precipitation on southwest side of the island rather than the station. As the cyclone moves east after 1200 UTC May

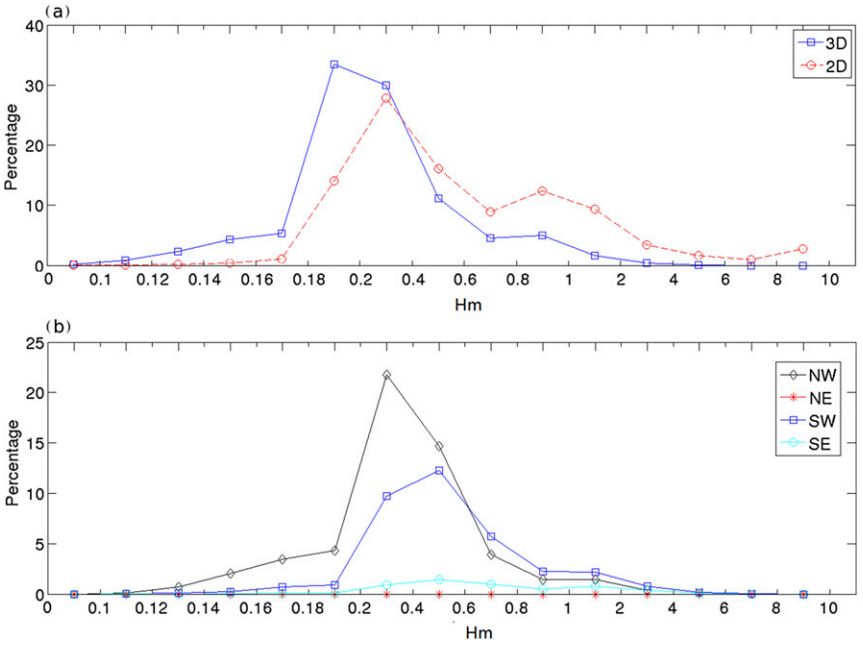

FIG. 14. (a) The probability density function (PDF) of nondimensional mountain height from the MAC soundings from 2003 to 2010. (b) The PDF of the 3D nondimensional mountain height for four 90° wind sectors at 850 hPa from the MAC soundings, with NW representing winds from 270° to 360°, etc.

6, the cold band reaches Macquarie Island, where the wind is normally from the south and southwest and precipitation decreases considerably (Fig. 13b). While specific differences exist between the simulations with and without terrain, there is a reasonable agreement.

5. Discussion

A climatology of the 2D and 3D nondimensional mountain heights has been produced from the MAC soundings from 2003 to 2010 (Fig. 14a). Most of the 3D nondimensional mountain heights are less than 1, which suggests that the 250-m ridge near the station does not strongly block the flow and motion across the ridge is common. For the 2D analysis, there are accordingly more cases with the nondimensional mountain height larger than 1 as the cross-mountain wind U_c is reduced. This suggests that the upstream blocking is more common upwind of the main part of the island away from the station.

The four case studies show that the orographic effects at the weather station depend on the wind directions and the nondimensional mountain height. We can infer that significant orographic effects could be found at the weather station, when winds are northwesterly, and the nondimensional mountain height is larger than 1, or when winds are southwesterly, and the nondimensional mountain height is less than 1. The former is very rare (1.4%) (Fig. 14b), while the latter is relatively common (33.6%), but normally associated with drizzle or no precipitation. Orographic effects on the precipitation records of the station in other cases are nearly negligible. For example, most frontal precipitation at MAC has been found associated with northwesterly winds and the nondimensional mountain height is less than 1, as shown in the cold- and warm-frontal cases (53.5%), which leads to minimal orographic effects on the precipitation observation at the station.

Our understanding of the orographic effects over Macquarie Island is limited by sparse observations and a generalization of the dominant meteorological conditions. Certainly extraordinary precipitation events do arise, as detailed in Wang et al. (2015). To further generalize the orographic effect on the precipitation records at MAC station, the 3-h surface records from MAC (and ERA-I) are presented (Fig. 15). [Note that a full precipitation rose is presented in Wang et al. (2015).] For the MAC records with northwesterly wind, no precipitation is observed 40% of the total time from 2003 to 2010, while precipitation is observed in 24% of the time. No significant orographic effect is expected on the surface precipitation at the station during this 64% of time. For the southwesterly wind sector, no precipitation is observed in 16% of the time, while precipitation is observed in 10% of the time. During these times orographic

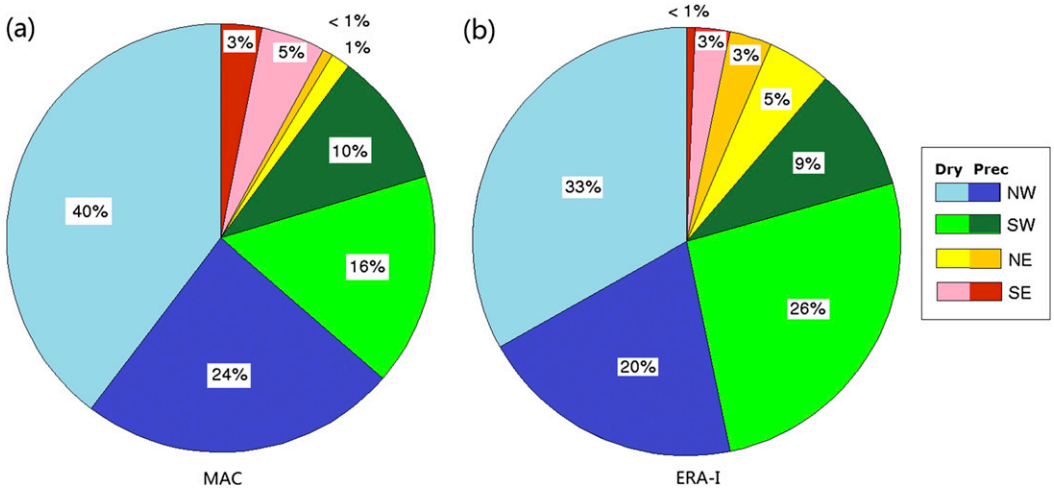

FIG. 15. Pie charts showing the frequency of winds from different sectors (as in Fig. 14) with (dark shades) and without (light shades) precipitation (2003–11) from (a) MAC and (b) ERA-I.

effects may be present at the station. Northeasterly and southeasterly winds are rare. For ERA-I, which does not include the terrain, southwesterly winds are more common, occurring 35% of the time. As discussed in Wang et al. (2015), this suggests that a portion of the southwesterly surface winds is forced around the ridge located to the southwest of the station.

6. Conclusions

To study the orographic forcing of Macquarie Island on the records of its weather station, four representative case studies—namely, a cold front, a warm front, drizzle, and a midlatitude cyclone—have been simulated using high-resolution numerical simulations both with and without terrain. Although the simulations of the precipitation and low-level clouds have limitations, this preliminary study shows that the orographic forcing on the precipitation record is not significant for most of these cases, with the exception of when drizzle is present in southwesterly winds. Ultimately, the station is well positioned for capturing many of the dominant meteorological conditions and is exposed to the most frequent precipitation events arriving from the north and west. The precipitation at the station can been perturbed when the air mass arrives from the south and southwest, although this is commonly associated with weak precipitation or drizzle during cold air advection.

Similarly, the orographic forcing on the surface winds is relatively weak near the station. The weakest forcing occurs when the winds are from the northwest. For the frontal cases simulated, the differences in wind speeds are less than $5\,m\,s^{-1}$ when the winds were from the west or northwest but were greater for southerly and southwesterly winds. The orographic effects on the pressure and temperature are not significant.

A climatology of the local soundings finds both the 2D and 3D nondimensional mountain height to be commonly below 0.5 and only rarely above 2. Blocking is not a common event at Macquarie Island, but this is not particularly surprising given the strong winds over the Southern Ocean and the limited height of the island (410 m). Consistent with the weak nondimensional mountain height, the simulations reveal an orographic effect in the lee of the island, with the enhancement of precipitation.

Similar to previous works simulating the boundary layer clouds over the Southern Ocean (Huang et al. 2014, 2015), these high-resolution WRF simulations have limited skill in generating boundary layer clouds, as observed by MODIS. Such clouds are common in a postfrontal environment and winds from the southwest. As concluded earlier, these are also the conditions when it is likely to have an orographic enhancement to weak precipitation or drizzle over the station.

While our limited evaluation process finds that the WRF simulations have captured the dominant meteorological conditions of the four case studies, it is still possible that other important precipitation processes (e.g., embedded convection or a seeder–feeder mechanism) have not been captured. Unfortunately, there is little means to either confirm or reject the presence of these processes.

If drone aircraft systems are to be used to investigate the dynamical processes and aerosol–cloud interactions around Macquarie Island in the future, the flow field distortion must be appreciated. As seen from the simulations with terrain, the gravity waves on the downwind side caused by the island could penetrate the tropopause with a vertical wind speed of $0.4\,m\,s^{-1}$ if

the wind is strong enough ($>15\,m\,s^{-1}$) and propagate horizontally more than 60 km if the wind direction does not change, which is consistent with the airborne observations in DEEPWAVE (Fritts et al. 2015).

Acknowledgments. This research was funded by Australian Research Council Linkage Grant LP120100115 and relies on datasets provided by the Australian Bureau of Meteorology. Three anonymous reviewers are gratefully acknowledged for their helpful comments.

REFERENCES

Adams, N., 2009: Climate trends at Macquarie Island and expectations of future climate change in the sub-Antarctic. *Pap. Proc. Roy. Soc. Tasmania*, **143**, 1–8.

Baines, P. G., 1998: *Topographic Effects in Stratified Flow*. Cambridge University Press, 482 pp.

Bates, T. S., and Coauthors, 1998a: Processes controlling the distribution of aerosol particles in the lower marine boundary layer during the First Aerosol Characterization Experiment (ACE 1). *J. Geophys. Res.*, **103**, 16 369–16 383, doi:10.1029/97JD03720.

——, B. J. Huebert, J. L. Gras, F. B. Griffiths, and P. A. Durkee, 1998b: International global atmospheric chemistry (IGAC) project's first aerosol characterization experiment (ACE 1): Overview. *J. Geophys. Res.*, **103**, 16 297–16 318, doi:10.1029/97JD03741.

Bodas-Salcedo, A., K. D. Williams, P. R. Field, and A. P. Lock, 2012: The surface downwelling solar radiation surplus over the Southern Ocean in the Met Office model: The role of midlatitude cyclone clouds. *J. Climate*, **25**, 7467–7486, doi:10.1175/JCLI-D-11-00702.1.

Boers, R., and P. B. Krummel, 1998: Microphysical properties of boundary layer clouds over the Southern Ocean during ACE 1. *J. Geophys. Res.*, **103**, 16 651–16 663, doi:10.1029/97JD03280.

——, J. B. Jensen, and P. B. Krummel, 1998: Microphysical and short-wave radiative structure of stratocumulus clouds over the Southern Ocean: Summer results and seasonal differences. *Quart. J. Roy. Meteor. Soc.*, **124**, 151–168, doi:10.1002/qj.49712454507.

Brown, R. A., 1980: Longitudinal instabilities and secondary flows in the planetary boundary layer: A review. *Rev. Geophys.*, **18**, 683–697, doi:10.1029/RG018i003p00683.

Browning, K. A., F. F. Hill, and C. W. Pardoe, 1974: Structure and mechanism of precipitation and the effect of orography in a wintertime warm sector. *Quart. J. Roy. Meteor. Soc.*, **100**, 309–330, doi:10.1002/qj.49710042505.

Cannon, D. J., D. J. Kirshbaum, and S. L. Gray, 2012: Under what conditions does embedded convection enhance orographic precipitation? *Quart. J. Roy. Meteor. Soc.*, **138**, 391–406, doi:10.1002/qj.926.

Catto, J. L., C. Jakob, G. Berry, and N. Nicholls, 2012: Relating global precipitation to atmospheric fronts. *Geophys. Res. Lett.*, **39**, L10805, doi:10.1029/2012GL051736.

Chen, F., and J. Dudhia, 2001: Coupling an advanced land surface–hydrology model with the Penn State–NCAR MM5 modeling system. Part I: Model implementation and sensitivity. *Mon. Wea. Rev.*, **129**, 569–585, doi:10.1175/1520-0493(2001)129<0569:CAALSH>2.0.CO;2.

Chubb, T. H., J. B. Jensen, S. T. Siems, and M. J. Manton, 2013: In situ observations of supercooled liquid clouds over the Southern Ocean during the HIAPER Pole-to-Pole Observation campaigns. *Geophys. Res. Lett.*, **40**, 5280–5285, doi:10.1002/grl.50986.

——, Y. Huang, J. B. Jensen, T. Campos, S. T. Siems, and M. J. Manton, 2016: Observations of high droplet number concentrations in Southern Ocean boundary layer clouds. *Atmos. Chem. Phys.*, **16**, 971–987, doi:10.5194/acp-16-971-2016.

Colle, B. A., 2004: Sensitivity of orographic precipitation to changing ambient conditions and terrain geometries: An idealized modeling perspective. *J. Atmos. Sci.*, **61**, 588–606, doi:10.1175/1520-0469(2004)061<0588:SOOPTC>2.0.CO;2.

Dee, D., and Coauthors, 2011: The ERA-Interim reanalysis: Configuration and performance of the data assimilation system. *Quart. J. Roy. Meteor. Soc.*, **137**, 553–597, doi:10.1002/qj.828.

Ellis, T. D., T. L'Ecuyer, J. M. Haynes, and G. L. Stephens, 2009: How often does it rain over the global oceans? The perspective from *CloudSat*. *Geophys. Res. Lett.*, **36**, L03815, doi:10.1029/2008GL036728.

Farr, T. G., and Coauthors, 2007: The Shuttle Radar Topography Mission. *Rev. Geophys.*, **45**, RG2004, doi:10.1029/2005RG000183.

Fritts, D. C., and Coauthors, 2015: The Deep Propagating Gravity Wave Experiment (DEEPWAVE): An airborne and ground-based exploration of gravity wave propagation and effects from their sources throughout the lower and middle atmosphere. *Bull. Amer. Meteor. Soc.*, **97**, 425–453, doi:10.1175/BAMS-D-14-00269.1.

Gras, J. L., 1995: CN, CCN and particle size in Southern Ocean air at Cape Grim. *Atmos. Res.*, **35**, 233–251, doi:10.1016/0169-8095(94)00021-5.

Hande, L. B., S. T. Siems, and M. J. Manton, 2012a: Observed trends in wind speed over the Southern Ocean. *Geophys. Res. Lett.*, **39**, L11802, doi:10.1029/2012GL051734.

——, ——, ——, and D. Belusic, 2012b: Observations of wind shear over the Southern Ocean. *J. Geophys. Res.*, **117**, D12206, doi:10.1029/2012JD017488.

——, ——, ——, and D. H. Lenschow, 2015: An evaluation of COSMIC radio occultation data in the lower atmosphere over the Southern Ocean. *Atmos. Meas. Tech.*, **8**, 97–107, doi:10.5194/amt-8-97-2015.

Hong, S. Y., and J. J. Lim, 2006: The WRF single-moment 6-class microphysics scheme (WSM6). *J. Korean Meteor. Soc.*, **42**, 129–151.

Hornberger, G. M., and Coauthors, 2014: Dynamic Earth: GEO Imperatives & Frontiers 2015–2020. NSF Advisory Committee for Geosciences Rep., 41 pp. [Available online at http://www.nsf.gov/geo/acgeo/geovision/nsf_acgeo_dynamic-earth-2015-20.pdf.]

Hoskins, B. J., and K. I. Hodges, 2005: A new perspective on Southern Hemisphere storm tracks. *J. Climate*, **18**, 4108–4129, doi:10.1175/JCLI3570.1.

Houze, R. A., 2012: Orographic effects on precipitating clouds. *Rev. Geophys.*, **50**, RG1001, doi:10.1029/2011RG000365.

Huang, Y., S. T. Siems, M. J. Manton, A. Protat, and J. Delanoë, 2012: A study on the low-altitude clouds over the Southern Ocean using the DARDAR-MASK. *J. Geophys. Res.*, **117**, D18204, doi:10.1029/2012JD017800.

——, ——, ——, and G. Thompson, 2014: An evaluation of WRF simulations of clouds over the Southern Ocean with A-Train observations. *Mon. Wea. Rev.*, **142**, 647–667, doi:10.1175/MWR-D-13-00128.1.

——, C. N. Franklin, S. T. Siems, M. Manton, T. Chubb, A. Lock, and A. Klekociuk, 2015: Evaluation of boundary-layer cloud forecasts over the Southern Ocean in a limited-area numerical weather prediction system using in situ, space-borne and

ground-based observations. *Quart. J. Roy. Meteor. Soc.*, **141**, 2259–2276, doi:10.1002/qj.2519.

Iacono, M. J., J. S. Delamere, E. J. Mlawer, M. W. Shephard, S. A. Clough, and W. D. Collins, 2008: Radiative forcing by long-lived greenhouse gases: Calculations with the AER radiative transfer models. *J. Geophys. Res.*, **113**, D13103, doi:10.1029/2008JD009944.

Johansson, B., and D. Chen, 2003: The influence of wind and topography on precipitation distribution in Sweden: Statistical analysis and modelling. *Int. J. Climatol.*, **23**, 1523–1535, doi:10.1002/joc.951.

Jovanovic, B., K. Braganza, D. Collins, and D. Jones, 2012: Climate variations and change evident in high-quality climate data for Australia's Antarctic and remote island weather stations. *Aust. Meteor. Oceanogr. J.*, **62**, 247–261.

Kanitz, T., P. Seifert, A. Ansmann, R. Engelmann, D. Althausen, C. Casiccia, and E. G. Rohwer, 2011: Contrasting the impact of aerosols at northern and southern midlatitudes on heterogeneous ice formation. *Geophys. Res. Lett.*, **38**, L17802, doi:10.1029/2011GL048532.

Kirshbaum, D. J., and D. R. Durran, 2004: Factors governing cellular convection in orographic precipitation. *J. Atmos. Sci.*, **61**, 682–698, doi:10.1175/1520-0469(2004)061<0682:FGCCIO>2.0.CO;2.

Kuettner, J. P., 1971: Cloud bands in the atmosphere. *Tellus*, **23**, 404–425, doi:10.1111/j.2153-3490.1971.tb00585.x.

Li, J. L., D. E. Waliser, G. Stephens, S. Lee, T. L'Ecuyer, S. Kato, and H. Y. Ma, 2013: Characterizing and understanding radiation budget biases in CMIP3/CMIP5 GCMs, contemporary GCM, and reanalysis. *J. Geophys. Res. Atmos.*, **118**, 8166–8184, doi:10.1002/jgrd.50378.

Ma, L. M., and Z. M. Tan, 2009: Improving the behavior of the cumulus parameterization for tropical cyclone prediction: Convection trigger. *Atmos. Res.*, **92**, 190–211, doi:10.1016/j.atmosres.2008.09.022.

Mace, G. G., R. Marchand, Q. Zhang, and G. Stephens, 2007: Global hydrometeor occurrence as observed by *CloudSat*: Initial observations from summer 2006. *Geophys. Res. Lett.*, **34**, L09808, doi:10.1029/2006GL029017.

Miglietta, M. M., and A. Buzzi, 2001: A numerical study of moist stratified flows over isolated topography. *Tellus*, **53A**, 481–499, doi:10.1111/j.1600-0870.2001.00481.x.

Mlawer, E. J., S. J. Taubman, P. D. Brown, M. J. Iacono, and S. A. Clough, 1997: Radiative transfer for inhomogeneous atmospheres: RRTM, a validated correlated-*k* model for the longwave. *J. Geophys. Res.*, **102**, 16 663–16 682, doi:10.1029/97JD00237.

Moncrieff, M. W., D. E. Waliser, M. J. Miller, M. A. Shapiro, G. R. Asrar, and J. Caughey, 2012: Multiscale convective organization and the YOTC virtual global field campaign. *Bull. Amer. Meteor. Soc.*, **93**, 1171–1187, doi:10.1175/BAMS-D-11-00233.1.

Morrison, A. E., S. T. Siems, M. J. Manton, and A. Nazarov, 2010: A modeling case study of mixed-phase clouds over the Southern Ocean and Tasmania. *Mon. Wea. Rev.*, **138**, 839–862, doi:10.1175/2009MWR3011.1.

Nugent, A. D., R. B. Smith, and J. R. Minder, 2014: Wind speed control of tropical orographic convection. *J. Atmos. Sci.*, **71**, 2695–2712, doi:10.1175/JAS-D-13-0399.1.

Platnick, S., M. D. King, S. A. Ackerman, W. P. Menzel, B. A. Baum, J. C. Riedi, and R. A. Frey, 2003: The MODIS cloud products: Algorithms and examples from *Terra*. *IEEE Trans. Geosci. Remote Sens.*, **41**, 459–473, doi:10.1109/TGRS.2002.808301.

Rasmussen, R. M., P. Smolarkiewicz, and J. Warner, 1989: On the dynamics of Hawaiian cloud bands: Comparison of model results with observations and island climatology. *J. Atmos. Sci.*, **46**, 1589–1608, doi:10.1175/1520-0469(1989)046<1589:OTDOHC>2.0.CO;2.

Reisner, J. M., and P. K. Smolarkiewicz, 1994: Thermally forced low Froude number flow past three-dimensional obstacles. *J. Atmos. Sci.*, **51**, 117–133, doi:10.1175/1520-0469(1994)051<0117:TFLFNF>2.0.CO;2.

Ryan, B. F., and K. J. Wilson, 1985: The Australian summertime cool change. Part III: Subsynoptic and mesoscale model. *Mon. Wea. Rev.*, **113**, 224–240, doi:10.1175/1520-0493(1985)113<0224:TASCCP>2.0.CO;2.

Schär, C., and D. R. Durran, 1997: Vortex formation and vortex shedding in continuously stratified flows past isolated topography. *J. Atmos. Sci.*, **54**, 534–554, doi:10.1175/1520-0469(1997)054<0534:VFAVSI>2.0.CO;2.

Simmonds, I., and K. Keay, 2000: Mean Southern Hemisphere extratropical cyclone behavior in the 40-Year NCEP–NCAR Reanalysis. *J. Climate*, **13**, 873–885, doi:10.1175/1520-0442(2000)013<0873:MSHECB>2.0.CO;2.

Skamarock, W. C., and J. B. Klemp, 2008: A time-split nonhydrostatic atmospheric model for weather research and forecasting applications. *J. Comput. Phys.*, **227**, 3465–3485, doi:10.1016/j.jcp.2007.01.037.

Smith, R. B., 1979: The influence of mountains on the atmosphere. *Advances in Geophysics*, Vol. 21, Academic Press, 87–230, doi:10.1016/S0065-2687(08)60262-9.

Smolarkiewicz, P. K., and R. Rotunno, 1989: Low Froude number flow past three-dimensional obstacles. Part I: Baroclinically generated lee vortices. *J. Atmos. Sci.*, **46**, 1154–1164, doi:10.1175/1520-0469(1989)046<1154:LFNFPT>2.0.CO;2.

Streten, N. A., 1988: The climate of Macquarie Island and its role in atmospheric monitoring. *Pap. Proc. Roy. Soc. Tasmania*, **122**, 91–106.

Thompson, G., P. R. Field, R. M. Rasmussen, and W. D. Hall, 2008: Explicit forecasts of winter precipitation using an improved bulk microphysics scheme. Part II: Implementation of a new snow parameterization. *Mon. Wea. Rev.*, **136**, 5095–5115, doi:10.1175/2008MWR2387.1.

Trenberth, K. E., and J. T. Fasullo, 2010: Simulation of present-day and twenty-first-century energy budgets of the southern oceans. *J. Climate*, **23**, 440–454, doi:10.1175/2009JCLI3152.1.

Vinoth, J., and I. R. Young, 2011: Global estimates of extreme wind speed and wave height. *J. Climate*, **24**, 1647–1665, doi:10.1175/2010JCLI3680.1.

Wang, Z., S. Siems, D. Belusic, M. Manton, and Y. Huang, 2015: A climatology of the precipitation over the Southern Ocean as observed at Macquarie Island. *J. Appl. Meteor. Climatol.*, **54**, 2321–2337, doi:10.1175/JAMC-D-14-0211.1.

Watson, C. D., and T. P. Lane, 2012: Sensitivities of orographic precipitation to terrain geometry and upstream conditions in idealized simulations. *J. Atmos. Sci.*, **69**, 1208–1231, doi:10.1175/JAS-D-11-0198.1.

——, and ——, 2014: Further sensitivities of orographic precipitation to terrain geometry in idealized simulations. *J. Atmos. Sci.*, **71**, 3068–3089, doi:10.1175/JAS-D-13-0318.1.

Wyngaard, J. C., 2004: Toward numerical modeling in the "terra incognita." *J. Atmos. Sci.*, **61**, 1816–1826, doi:10.1175/1520-0469(2004)061<1816:TNMITT>2.0.CO;2.